Terahertz Magnetospectroscopy of Cyclotron Resonances from Topological Surface States in Thick Films of $Cd_xHg_{1-x}Te$

*Maximilian Otteneder, Daniel Sacré, Ivan Yahniuk, Grigory V. Budkin,
Kilian Diendorfer, Dmitry A. Kozlov, Ivan A. Dmitriev, Nikolay N. Mikhailov,
Sergey A. Dvoretsky, Vasily V. Bel'kov, Wojciech Knap, and Sergey D. Ganichev**

Herein, studies of the cyclotron resonance (CR) in thick $Cd_xHg_{1-x}Te$ films with different cadmium contents corresponding to materials with and without band inversion, as well as critical content corresponding to an almost linear energy dispersion are presented. The results demonstrate that the formation of 2D topological surface states requires sharp interfaces between layers with and without band inversion, in which case the corresponding CR is clearly observed for the out-of-plane orientation of magnetic field but does not show up for an in-plane orientation. In contrast, all samples having more conventional technological design with smooth interfaces (i.e., containing regions of $Cd_xHg_{1-x}Te$ with gradually changing Cd content x) show equally pronounced CR in both in-plane and out-of-plane magnetic field revealing that CR is excited in effectively 3D states. Modeling of the surface states for different film designs supports main observations. In all samples, additional broad helicity-independent resonances are observed, which are attributed to photoionization and magnetic freeze-out of impurity states.

1. Introduction

The discovery of the quantum spin Hall effect in HgTe quantum wells [1,2] and of topological insulators [3–5] stimulated rapidly growing interest in fundamental properties and possible applications of HgTe-based materials. An attractive feature of these materials is that the band inversion, crucial for the formation of time-reversal symmetry-protected gapless states, can be obtained in several different ways. In particular, the topological phase transition can be realized via the variation of the thickness of HgTe quantum wells, by changing temperature, or by applying strain. This, together with a high quality of materials grown by molecular beam epitaxy (MBE), provides unique opportunities to study helical Dirac fermions (for reviews, see, e.g., refs. [5,6]) as well as induced superconductivity and phase-controlled Josephson junctions.[7,8] Due to their specific energy dispersion, HgTe quantum wells and strained bulk films have revealed fascinating effects in magnetotransport [2,9] (for recent achievements, see refs. [10–19]), as well as in magneto- and terahertz-spectroscopy.[20–30]

More recently, a considerable attention has been attracted to bulk $Cd_xHg_{1-x}Te$ films with the Cd content x equal or lower than the critical one, x_c, defining the phase transition from inverted to noninverted band order.[31] This interest has been driven by the observation of 3D massless Kane fermions in films with $x = x_c$,[32] followed by detailed studies using magneto- and terahertz-spectroscopy.[33–35] Topological insulators (TIs) based on bulk films with Cd contents below

M. Otteneder, D. Sacré, K. Diendorfer, I. A. Dmitriev, S. D. Ganichev
Terahertz Center
University of Regensburg
93040 Regensburg, Germany
E-mail: Sergey.Ganichev@physik.uni-regensburg.de

I. Yahniuk, W. Knap
CENTERA Laboratories
Institute of High Pressure Physics
Polish Academy of Sciences
PL-01142 Warsaw, Poland

The ORCID identification number(s) for the author(s) of this article can be found under https://doi.org/10.1002/pssb.202000023.

G. V. Budkin, I. A. Dmitriev, V. V. Bel'kov
Ioffe Institute
194021 St. Petersburg, Russia

D. A. Kozlov, N. N. Mikhailov, S. A. Dvoretsky
Rzhanov Institute of Semiconductor Physics
630090 Novosibirsk, Russia

W. Knap
Laboratoire Charles Coulomb
University of Montpellier and CNRS
F-34095 Montpellier, France

the temperature-dependent critical x_c remain less studied so far.[36,37] These materials, however, have a number of advantages with respect to HgTe TIs. As demonstrated by Tomaka et al.,[36] the topologically protected surface states in $Cd_xHg_{1-x}Te$ are characterized by 1) two times higher Dirac fermion velocity (approximately the same as in graphene) than in pure HgTe, and 2) a larger band gap and a higher position of the Dirac point on the energy scale than that obtained in strained HgTe films. These significant advantages make TIs based on HgCdTe alloys promising for future applications.

Herein, we present a detailed study of terahertz cyclotron resonances (CRs) of thick undoped films observed in transmission, photocurrent,[25,38] and photoconductivity.[39] The films under study are characterized by different values of the Cd content x, corresponding to both normal and inverted band order. In all samples with band inversion, two CRs have been observed in the Faraday configuration, where both magnetic field and laser beam are oriented perpendicular to the sample surface. Evolution of these two distinct resonances with radiation frequency and helicity dependencies of the resonance amplitudes allow us to conclude that they represent CRs produced by two kinds of negatively charged carriers with slightly different masses. The cyclotron masses (below 0.01 m_0), obtained from the positions of the CRs, may be attributed to both bulk electrons and electrons in topological surface states, which are expected to exist in films with band inversion.

Our central observations come from CR measurements in Voigt configuration, still with normally incident THz radiation, but with a static magnetic field applied parallel to the sample surface. In this geometry, we obtain qualitatively different results for films with abruptly changing and gradually varying Cd content x at the interfaces between layers with and without band inversion. The combination of measurements with magnetic field applied in-plane and out-of-plane provides an unequivocal experimental test on whether 2D or 3D carriers are responsible for the observed CRs. While samples with smoothly varying x manifest almost identical resonant behavior in Faraday and Voigt configurations, in the sample with an abrupt transition to the cap layer one of the electron CRs disappears in the Voigt geometry. This observation clearly indicates a 2D nature of one group of electrons, apparently located at the abrupt interface and associated with a topological surface state. These conclusions are supported by theoretical modeling of the edge states in the films with abrupt and smooth interfaces. Therefore, the presence of a sharp interface appears to be a crucial technological requirement for studies of fundamental topological properties of such structures.

In samples without band inversion, we detect only one CR, with a CR mass close to that calculated for the bulk material. In all studied films, we also observe an additional broad resonance located in higher magnetic fields. This helicity-independent resonance manifests slower kinetics and decays rapidly with temperature. We assign this resonance to photoionization and magnetic freeze-out of impurity states.

2. Samples

The investigated samples are MBE-grown $Cd_xHg_{1-x}Te$ films having a common general layer structure shown in **Figure 1**.
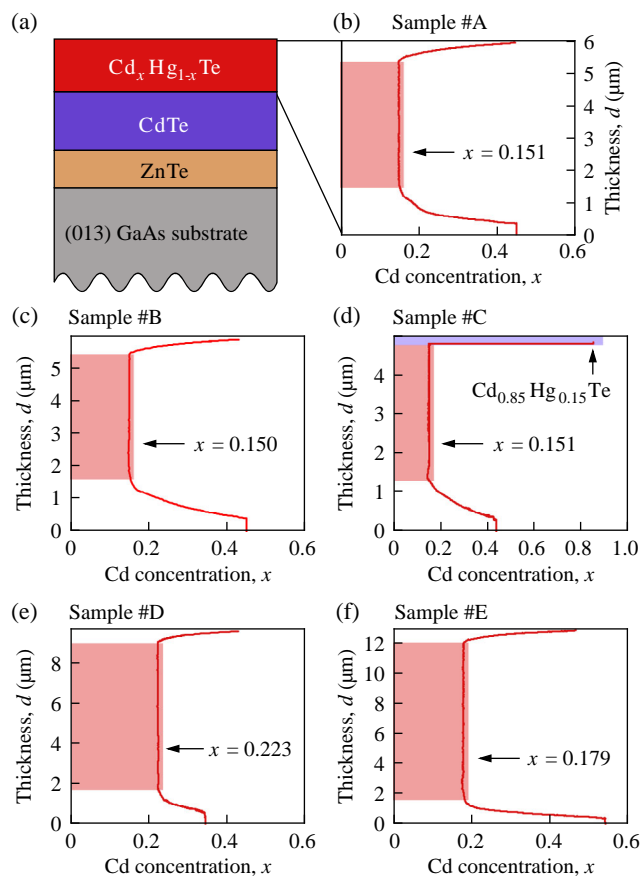

Figure 1. a) Schematic layer structure of all investigated $Cd_xHg_{1-x}Te$ films. b–f) The Cd content profile $x(d)$ in the top layer as a function of the distance d from the top of the preceding CdTe layer. The values of x in the flat region between interfaces are indicated in the corresponding panels. Note that unlike other structures with smoothly varying $x(d)$, the sample #C in part (d) has a sharp interface between the flat region made of $Cd_{0.15}Hg_{0.85}Te$ with band inversion and a 30 nm cap layer made of $Cd_{0.85}Hg_{0.15}Te$ without band inversion.

For each sample, a 30 nm ZnTe buffer layer was grown on top of a (013)-oriented GaAs substrate, followed by a 6 µm layer of CdTe. After that, $Cd_xHg_{1-x}Te$ films with different composition (as described later) and thickness ranging between 5 and 12 µm were fabricated. All wafers were cleaved into square 5×5 mm² samples. Ohmic indium contacts have been soldered to the sample edges and corners. In addition, for detailed magnetotransport studies, Hall bar samples were fabricated from several wafers.

Figure 1b–f shows the cadmium content x in $Cd_xHg_{1-x}Te$ films selected for the presentation as a function of the distance d from the top of the preceding CdTe layer. In the initial step of growth of the film ($d \lesssim 1.5$ µm), the cadmium content x was gradually decreased to reduce the strain related to a lattice mismatch, as well as to avoid possible interface disorder effects. Such smooth interfaces with varying x are conventionally used to improve optoelectronic and transport properties of $Cd_xHg_{1-x}Te$ films, which are widely used for the detection of infrared radiation. The region of varying x is followed by a wide region with constant $x = 0.15$ (samples #A, #B, and #C), $x = 0.18$ (sample #D),

or $x = 0.22$ (sample #E) which will be called the flat region in the following. After that, a cap layer with gradually increasing Cd content was grown in all samples except for the sample #C. In sample #C, the flat region with $x = 0.15$ was capped by a 30 nm layer of $Cd_{0.85}Hg_{0.15}Te$, which resulted in a sharp boundary between the flat region with band inversion and the cap layer without band inversion.

All samples were characterized by transport measurements performed using standard low-frequency lock-in technique in the temperature range from 2 to 300 K and an out-of-plane magnetic field up to 10 T. For wafers with no Hall bars available, the corresponding longitudinal and Hall resistivities have been calculated from data obtained on the van der Pauw samples using permutation method. These studies established that all samples exhibit similar transport behavior that is apparently insensitive to the presence of band inversions and to the type of interfaces. At low temperatures, all samples show strong positive magnetoresistance and a nonlinear Hall effect. A typical example is shown in **Figure 2** showing the longitudinal and Hall resistivities obtained from the magnetoresistance data recorded on a Hall bar sample made from wafer #A. The slope of the Hall resistivity at low magnetic field corresponds to negatively charged carriers (electrons), whereas at strong field the Hall slope typically changes to a hole-like. Such behavior is conventional for electron–hole systems[40] in conditions when the hole density exceeds the electron density (although both have the same order of magnitude), whereas electrons are characterized by a significantly higher mobility. The values of sheet densities and mobilities for different types of carriers can be extracted using the two-component classical Drude model, which was successfully implemented for thin HgTe films.[11,38,41] The values of sheet electron density n_s obtained from such modeling are shown in **Table 1**. In this table, we also provide the values of average volume electron density n, which are obtained from the corresponding sheet electron densities n_s as $n = n_s/w$, where w denotes the corresponding $Cd_xHg_{1-x}Te$ film thicknesses (Figure 1b–f).

It should be emphasized that the aforementioned technique does not allow one to distinguish possible different groups of electrons (or holes) and yields the total electron and hole densities and average mobilities only. We also mention that the agreement between measured transport data and fits using the two-component model was not very good in the region of low magnetic fields. Therefore, in Figure 2d, we present results of an alternative simpler treatment within the single-component Drude model, where the effective sheet density of electrons in the film n_s is obtained from the linear slope of the Hall resistivity at low magnetic fields.

Overall, transport measurements demonstrate that, at low temperatures, the electron sheet density is rather small and lies in a range of $n_s = 2 \div 4 \times 10^{11}$ cm^{-2}. The hole sheet density is slightly larger than the electron one. The holes do not contribute to the observed CRs, so their properties will not be discussed in detail. However, they play an important role in keeping the overall electroneutrality. At higher temperatures, both electron and hole densities increase, mainly because of the usual temperature smearing of the energy distribution, but temperature variation of the bulk energy gap may also play an important role.[33] Typically, at 77 K, the electron sheet density reaches $n_s = 2 \div 3 \times 10^{12}$ cm^{-2} for all samples, whereas at 300 K the density rises to $n_s = 3 \times 10^{13} \div 1.2 \times 10^{14}$ cm^{-2}. It is worth noting that at liquid nitrogen temperature every sample shows an order of magnitude increase in density in comparison with low temperatures, and, at the same time, the values of n_s are very similar for all samples independent of the value of the band gap in the flat region. Such behavior suggests that at $T < 77$ K, the bulk carriers do not play any essential role in transport and points to the formation of inversion/accumulation quasi-2D layers at the interfaces of the film, or, alternatively, to the formation of topological surface states with similar properties in samples with band inversion. Note that in both cases the bulk holes play an important role in maintaining overall charge neutrality in the sample.
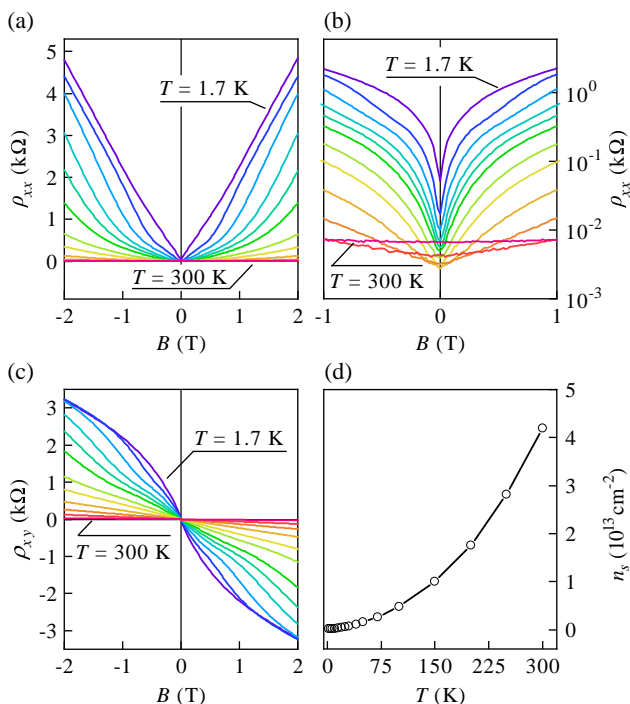

Figure 2. Magnetoresistivity obtained on a Hall bar made from wafer #A with $x = 0.15$ at different temperatures, $T = 1.7, 10, 15, 20, 25, 30, 40, 50, 70, 100, 150$, and 300 K. a,b) The longitudinal sheet resistivity ρ_{xx} in linear and logarithmic scale, respectively. c) The Hall resistivity ρ_{xy}. d) The effective sheet electron density $n_s(T)$ obtained from the linear slope of ρ_{xy} at $B = 0$ in part (c).

Table 1. Basic parameters of the investigated samples #A– #E including the Cd content x, the corresponding type of the band order in the flat region, type of the top interface, the effective sheet electron density n_s obtained from low-frequency magnetotransport measurements at $T = 4.2$ K, and the corresponding average volume density n (obtained as n_s divided by the total $Cd_xHg_{1-x}Te$ film thickness).

Sample	Cd content, x	Band structure	Top interface	$n_s [10^{11} cm^{-2}]$	$n [10^{14} cm^{-3}]$
#A	0.151	Inverted	Smooth	2.9	4.8
#B	0.150	Inverted	Smooth	2.2	3.7
#C	0.151	Inverted	Sharp	3.3	6.7
#D	0.179	Normal	Smooth	4.2	4.2
#E	0.223	Normal	Smooth	2.4	1.9

2000023 (3 of 13)

3. Methods

For optical excitation, we used linearly polarized radiation from a continuous wave molecular gas laser operating at frequencies $f = 2.54\,THz$ (wavelength $\lambda = 118\,\mu m$, photon energy $\hbar\omega = 10.5\,meV$), $1.63\,THz$ ($\lambda = 184\,\mu m$, $\hbar\omega = 6.74\,meV$), and $0.69\,THz$ ($\lambda = 432\,\mu m$, $\hbar\omega = 2.87\,meV$).[40,42] The laser provided radiation power ranging between 40 and $120\,mW$ depending on the wavelength. The radiation was modulated by an optical chopper operating at a frequency of about $80\,Hz$. The samples were placed in a temperature controllable optical cryostat with z-cut quartz and polymethylpentene windows. To block visible and near-infrared radiation, the windows were additionally covered by black polyethylene foil. The laser beam was focused using off-axis parabolic mirrors and controlled by a pyroelectric camera.[43] It had an almost Gaussian shape with the spot diameter ranging from 1.5 to $3\,mm$ depending on the wavelength. Room-temperature lambda plates made of x-cut quartz were used to modify the state of polarization, in particular, to obtain circularly polarized right-handed (σ^+) and left-handed (σ^-) radiation. For time-resolved measurements, we additionally used a pulsed optically pumped THz laser with a pulse duration of about $100\,ns$, a repetition rate of $1\,Hz$, and a peak power P of up to $60\,kW$.[44–46] The laser emitted frequency lines in the range between 0.6 and $2.6\,THz$.

A split coil superconductive magnet was used to study magnetic field dependencies of radiation transmission and photocurrents. Most of the experiments were performed with normally incident THz radiation and magnetic field oriented either perpendicular to the film surface (Faraday geometry) or in-plane (Voigt geometry) (**Figure 3**a,b). In addition, experiments in Faraday geometry with the sample tilted by an angle θ were conducted (Figure 3c).

For experiments on radiation transmission, a pyroelectric detector was placed behind the sample (Figure 3). Photovoltage and photoconductivity measurements were conducted using a standard lock-in technique. Photovoltage was measured using the phase-locked voltage drop across the sample under the influence of the chopper-modulated THz radiation in the absence of external DC bias. To measure the photoconductivity, an external DC bias was applied and photoresponses for positive and negative bias polarities were subtracted to exclude photogalvanic contributions and extract the photoconductivity signal. Alternatively, in some photoconductivity measurements, we applied a low-frequency AC bias and used a double-modulation technique described in previous studies.[39,47]

Because main conclusions of this work are based on the comparison of results obtained using the three setups in Figure 3, it is important to recall the basic distinctions between them in application to 3D and 2D electron systems. In a 3D system, CR is expected to emerge in all three setups; the orientation of both the laser beam and static magnetic field with respect to the sample surface is immaterial for a 3D isotropic system; the dynamics of carriers is different for parallel (Faraday) and perpendicular (Voigt) relative orientation of the magnetic field and THz radiation propagation directions. This different dynamics may lead to a substantial shift of the resonance position in Voigt geometry with respect to Faraday geometry (see ref. [48] and Section 5 for details).

For a 2D system localized at an interface parallel to the sample surface, the decisive role is played by the orientation of the magnetic field with respect to the surface. Only the normal component of the magnetic field affects the in-plane dynamics of carriers and leads to the development of the cyclotron motion and the formation of Landau levels. In contrast, the in-plane static magnetic field can only slightly modify the confinement energy and the corresponding common wave function describing the localized 2D electron states. In the case of normal orientation of magnetic field (as in Faraday geometry in Figure 3a), one thus expects a usual CR dip in transmission for both 2D and 3D electrons. On the contrary, for in-plane magnetic field (as in Voigt geometry in Figure 3b) 2D electrons should manifest no CR, whereas 3D electrons can still experience CR.
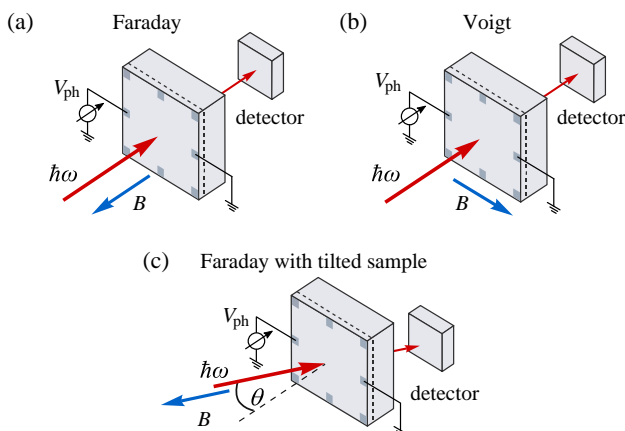
4. Results

4.1. Cyclotron Resonances in $Cd_{0.15}Hg_{0.85}Te$ Films with Band Inversion and Smooth Interfaces

We begin with the presentation of results of magnetotransmission and photovoltage measurements performed on almost identical $Cd_{0.15}Hg_{0.85}Te$ films #A and #B (Figure 1b,c). The flat layer in both samples has a Cd content $x \simeq 0.15$, corresponding to inverted bands for temperatures below $T \simeq 90\,K$.[33] On both sides of the flat layer, the Cd content gradually increases, thus providing smooth interfaces to regions without band inversion. Magnetotransmission data recorded in Faraday geometry (Figure 3a) for samples #A and #B are presented, correspondingly, in **Figure 4** and **Figure 5**. The data here and later generally manifest three resonant dips for both negative and positive values of the out-of-plane magnetic field B. The positions of observed resonances at $B = \pm B_{CR1,2}$, $B = \pm B_{CR}$, and $B = \pm B_i$, marked by arrows in Figures 4 and 5, are always symmetrically offset from the origin $B = 0$.

Figure 3. Experimental setups for transmission and photovoltage measurements: a) Faraday configuration with both magnetic field and the incident THz beam oriented along the normal to the sample surface; b) Voigt configuration with an in-plane magnetic field; c) Faraday configuration with the sample being tilted by an angle θ with respect to the common direction of the laser beam and magnetic field.
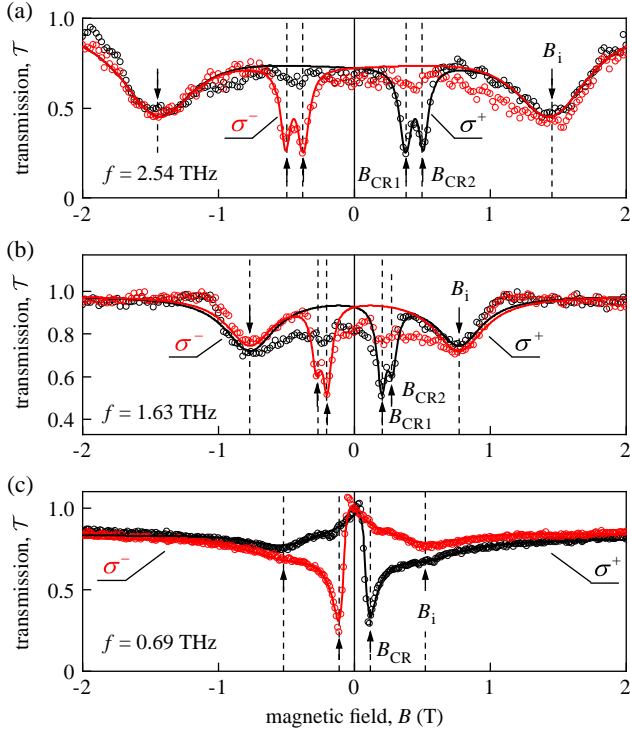
Figure 4. Magnetotransmission normalized to its maximal value for sample #A with band inversion in the flat region. Measurements were done in Faraday geometry (Figure 3a) at $T = 4.2$ K using σ^+ and σ^- polarized radiation at three different frequencies: a) $f = 2.54$ THz, b) $f = 1.63$ THz, and c) $f = 0.69$ THz. In all panels, the experimental data points are shown by circles, whereas the solid lines present the fits described in the text. In all cases, we observe sharp deep minima at positions of CRs [$B = \pm B_{CR1}$ and $B = \pm B_{CR2}$ in (a,b), and $B = \pm B_{CR}$ in (c)], see arrows marked at the positive B side. These CRs show up at either positive or negative B depending on the helicity of incoming radiation. At higher B, we observe symmetric wide minima centered at $B = \pm B_i$, which are not sensitive to the radiation helicity. The resonance field values and corresponding cyclotron masses are shown in Table 2.

The main focus of this work concerns the sharp dips at low B which, as shown later, originate from the CR of free conduction electrons. In contrast, the broad minima at $B = \pm B_i$ are attributed to photoionization of impurities and will be addressed separately in Section 4.4. The data in Figures 4 and 5a show that the low-field resonances are sensitive to the radiation helicity. Although, for the right-handed circular polarization σ^+, they appear only at positive B, for the left-handed circular polarization σ^-, they are present at negative B only. The position of these resonances scales linearly with the radiation frequency (Figure 5b). All these features indicate that the low-B sharp dips are indeed caused by the CR of negatively charged free carriers.

More specifically, magnetotransmission traces in Figure 4a that were recorded at the highest radiation frequency $f = 2.54$ THz show two distinct sharp dips at $B = \pm B_{CR1}$ and $B = \pm B_{CR2}$, which clearly reveals the presence of two kinds of electrons with different cyclotron masses (the corresponding values are shown in **Table 2**). It is worth mentioning at this point that the corresponding cyclotron masses below 0.01 m_0 may be attributed
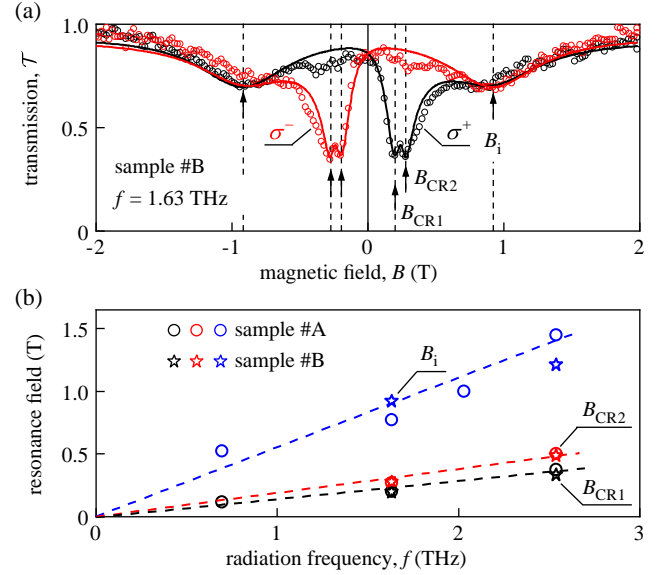

Figure 5. a) Normalized magnetotransmission of $f = 1.63$ THz radiation measured on sample #B in Faraday geometry at $T = 4.2$ K. Two well-resolved CR dips emerge at either $B = B_{CR1,2}$ or $B = -B_{CR1,2}$ depending on the helicity (σ^+ or σ^-) of incoming radiation. Additional helicity insensitive resonances are detected at $B = \pm B_i$ in both traces. Solid lines are fits according to Equation (2) including additional Lorentzians at $\pm B_i$. b) Magnetic field positions of the observed resonances B_{CR1}, B_{CR2}, and B_i (as marked) plotted against radiation frequency for samples #A (circles) and #B (stars) (see also Table 2). Dashed lines present linear fits to the data.

both to bulk electrons and electrons in topological surface states, which are expected to exist in the films with inverted bands. At lower frequency $f = 1.63$ THz, the CR dips start to merge, and become indistinguishable at the lowest frequency $f = 0.69$ THz where a single merged CR dip B_{CR} is observed (Figure 4b,c). The positions of the resolved CR dips for $f = 2.54$ THz and $f = 1.63$ THz are found to be almost identical for both samples #A and #B (Figures 4 and 5 and Table 2).

Solid lines in Figure 4 show magnetotransmission fits obtained using a two-component Drude model with account for interference effects due to multiple reflections in the substrate. Specifically, the complex THz conductivity σ is modeled as a sum of contributions σ_j from each electron transport channel j, with individual σ_j given by the Drude formula

$$\sigma_j = \frac{e n_{sj}}{\mu_j^{-1} + i(B_{CRj} \pm B)} \tag{1}$$

Here, e is the elementary charge, n_{sj} and μ_j are the electron sheet density and mobility in the transport channel j, $B_{CRj} = m_j 2\pi f/e$ defines the position of CR for a given THz frequency f through the cyclotron mass m_j, and the $+ (-)$ sign before B corresponds to the left-handed (right-handed) circular polarization of the THz radiation. The fraction of transmitted power in Faraday geometry is then expressed through $\tilde{\sigma} = \sigma/2\epsilon_0 c$ as [49,50]

$$T(B) = \left| (1 + \tilde{\sigma}) \cos\phi - i \frac{1 + n_r^2 + 2\tilde{\sigma}}{2 n_r} \sin\phi \right|^{-2} \tag{2}$$

Table 2. Magnetic-field positions of resonances and corresponding cyclotron masses extracted from magnetotransmission and photovoltage traces obtained at $T = 4.2$ K. Note that resonances marked with an asterisk were visible in photovoltage only, and were not resolved in magnetotransmission.

Sample	Cd content x	Frequency, f [THz]	B_{CR1} [T] or B_{CR} [T]	B_{CR2} [T]	B_i [T]	B_{CR1}^V [T] or B_{CR}^V [T]	B_{CR2}^V [T]	m_{CR1} [m_e]	m_{CR2} [m_e]
#A	0.15	2.54	0.38	0.50	1.45			0.0042	0.0055
		1.63	0.20	0.27	0.77	0.16	0.24	0.0035	0.0046
		0.69	0.09*	0.11	0.52*			0.0035	0.0044
#B	0.15	2.54	0.33	0.49	1.25	0.36	0.50	0.00365	0.0053
		1.63	0.20	0.28	0.92	0.20	0.28	0.0034	0.0047
#C	0.15	2.54	0.30	0.46	1.35*	0.46	–	0.0033	0.0051
#D	0.22	2.54	0.81	–	2.33*	0.82	–	0.0089	–
		1.63	0.49	–	1.45*	0.45	–	0.0084	–
#E	0.18	2.54	0.28	–	0.77*			0.0031	–
		0.69	0.065	–	0.25*			0.0026	–

where ϕ is the interference phase accumulated after single reflection in the substrate, n_r is the refractive index of the substrate, ε_0 the permittivity of free space, and c the speed of light. Using Equation (2), we were able to precisely fit all magnetotransmission traces. This demonstrates that the model based on Drude approximation is capable to reproduce the experimental observations. At the same time, the magnetotransmission traces do not provide sufficient data to convincingly extract all relevant parameters of the model. The fits to experimental data required an additional constant offset accounting for nonresonant contributions of other transport channels. Two identical Lorentzians centered at $B = \pm B_i$ were included into the model to account for the impurity resonances discussed in Section 4.4.

The CRs were also detected in photovoltage experiments. A typical photovoltage trace, shown in the inset of **Figure 6**a, features two peaks coinciding with the positions of the CR dips in magnetotransmission as indicated by vertical dashed lines. Similar to the transmission dips, the position of the peaks scales linearly with the radiation frequency (Figure 6a). Note that, in the photovoltage response, two CR peaks are clearly resolved even for the lowest frequency $f = 0.69$ THz, in which case the CR dips in magnetotransmission get merged (Figure 4c).

Strikingly, applying a tilted magnetic field (see the experimental setup in Figure 3c), we obtain that the CR positions are independent of the tilt angle θ (Figure 6b). This observation provides a first clear evidence that the resonances are excited in a 3D electron gas. Indeed, for a 2D system, one would expect a significant up-shift of the resonance position with the increase in the tilt angle because in this case the CR should be sensitive only to the normal component of the magnetic field. Here, it is important to stress that the tilted field measurements are performed in Faraday geometry, in which case the resonance position for an isotropic 3D system is expected to be independent of the tilt angle.

Measurements of the magnetotransmission in Voigt geometry (Figure 3b) confirm the aforementioned conclusions showing that even for a magnetic field oriented in-plane both CRs are still present (**Figure 7**). This observation rules out the possibility that any of the observed resonances originates from 2D electrons.

We note that, as expected, in Voigt geometry, the CR dips become helicity-independent and show up symmetrically for two polarities of magnetic field. The CR field values detected for sample #A are found to be slightly smaller in Voigt geometry than in Faraday geometry, which could be attributed to the 3D
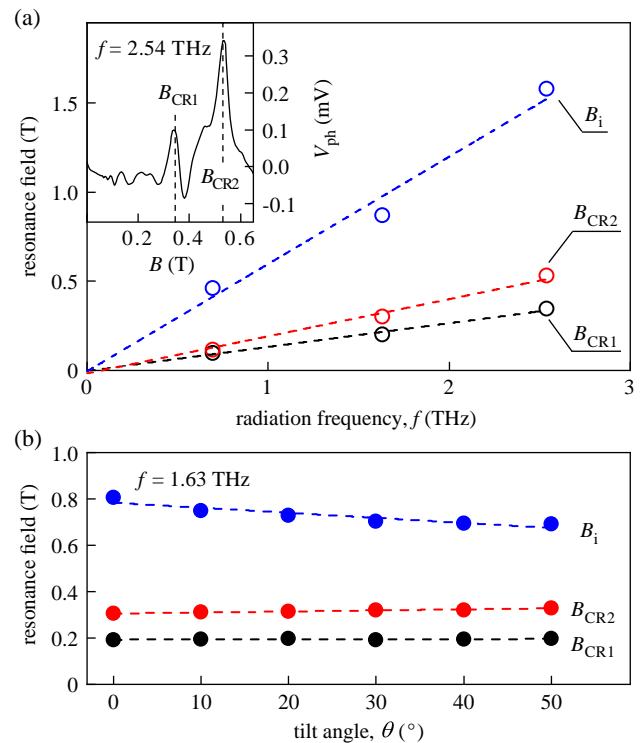

Figure 6. a) Resonance field values B_{CR1}, B_{CR2}, and B_i (as marked) extracted from photovoltage measurements on sample #A at $T = 4.2$ K in Faraday configuration. The low-B part of a typical photovoltage trace, obtained at radiation frequency $f = 2.54$ THz, is shown in the inset. b) Dependence of the resonance field values on the tilt angle obtained from photovoltage measurements on sample #A at $T = 4.2$ K under $f = 1.63$ THz radiation in the Faraday configuration with tilted sample (Figure 3c). Dashed lines are linear fits to the data.
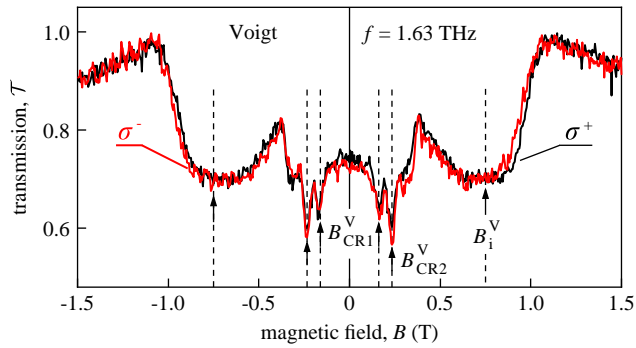
Figure 7. Normalized magnetotransmission of $f = 1.63$ THz radiation measured in Voigt configuration on sample #A at $T = 4.2$ K. Two pairs of well resolved CR dips emerge symmetrically at $B = B_{CR1,2}^V$ and $B = -B_{CR1,2}^V$ for both circular polarizations σ^+ (black curve) and σ^- (red curve). Additional broad resonances are detected at $B = \pm B_i$ in both traces. All resonance field values are shown in Table 2.

plasmonic shift (see ref. [48] and Section 5). Surprisingly, such shifts were not detected for other samples (Table 2).

4.2. Cyclotron Resonances in $Cd_{0.15}Hg_{0.85}Te$ Film with Band Inversion and Sharp Top Interface

For sample #C, the behavior of resonances becomes qualitatively different despite the fact that this sample has almost the same design and that the Cd content in the flat region remains the same as in samples #A and #B. The only difference is that, instead of a smooth top interface as in samples #A and #B, sample #C has an abrupt boundary between the $Cd_{0.15}Hg_{0.85}Te$ film and the $Cd_{0.85}Hg_{0.15}Te$ cap layer (Figure 1d).

Similar to samples #A and #B, in Faraday geometry, sample #C clearly manifests two CRs in both magnetotransmission (see, e.g., blue curve in **Figure 8**a) and photovoltage (Figure 8c). However, in sharp contrast to samples with two smooth interfaces, in Voigt configuration only one CR dip remains (Figure 8b). The fact that one of the resonances disappears in Voigt geometry provides a clear evidence that it originates from 2D confined electron states. Figure 8d shows the temperature dependence of the dip amplitude $\Delta\mathcal{T}$. For resonances at B_{CR1} (Faraday geometry) and B_{CR}^V (Voigt configuration), we observe that $\Delta\mathcal{T}$ is almost independent of temperature. In contrast, the strength of the CR resonance at B_{CR2}, which is present in Faraday geometry only, strongly increases with rising temperature. Such temperature evolution is strikingly similar to that found recently for topological surface states in strained 80 and 200 nm HgTe films.[25,38] Taken together, the aforementioned observations clearly indicate the formation of 2D surface states at the abrupt interface between materials with and without band inversion.

4.3. Cyclotron Resonances in Films without Band Inversion

We proceed to results obtained on films #D (with $x = 0.22$) and #E ($x = 0.18$) which are expected to have normal band order. Indeed, the data we are going to discuss were obtained at liquid helium temperature at which the critical Cd content marking the
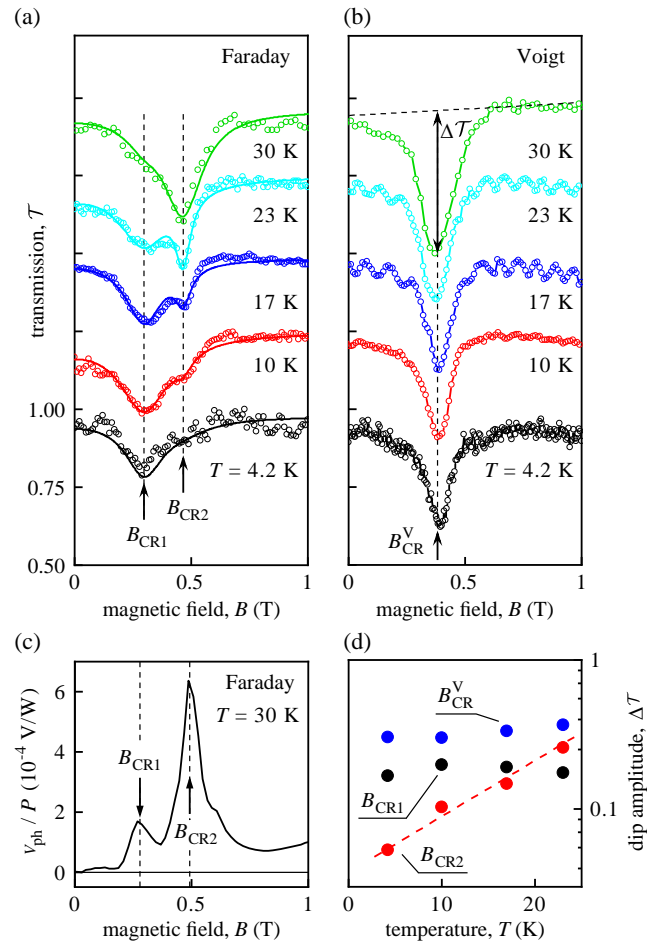

Figure 8. Normalized magnetotransmission of $f = 2.54$ THz radiation obtained on sample #C at different temperatures (as marked) in a) Faraday and b) Voigt configurations. Traces are vertically offset by 0.25 for better visibility. Solid lines in part (a) are fits using Equation (2). c) Photovoltage measured on sample #C in Faraday configuration at $T = 30$ K. d) Temperature dependence of the amplitudes $\Delta\mathcal{T}$ of the CR dips at $B_{CR1,2}$ and B_{CR}^V (as marked) extracted from the magnetotransmission data presented in parts (a) and (b). The dashed line shows a linear fit for the amplitude of the CR dip at B_{CR2}. The corresponding CR field values are shown in Table 2.

transition from normal to inverted band order is $x_c \simeq 0.17$.[33,51] Thus, in both samples, the Cd content in the flat region is higher than x_c meaning that they should behave as conventional narrow-gap semiconductors.

In contrast to previously discussed materials with $x = 0.15$, for these samples, we observe a single CR in both Faraday and Voigt geometries. Magnetotransmission data for samples #D and #E is shown in **Figure 9**a,b and **Figure 10**a. The data in Figure 9a,b are obtained with linearly polarized THz radiation. Correspondingly, the CR dip is present for both polarities of magnetic fields. For circularly polarized radiation, the CR dip appears either in positive (σ^+) or negative (σ^-) B (Figure 10a).

It is worth mentioning that the CR positions and the corresponding cyclotron masses obtained on samples #D and #E (see Table 2 and insets in Figures 9 and 10) are substantially
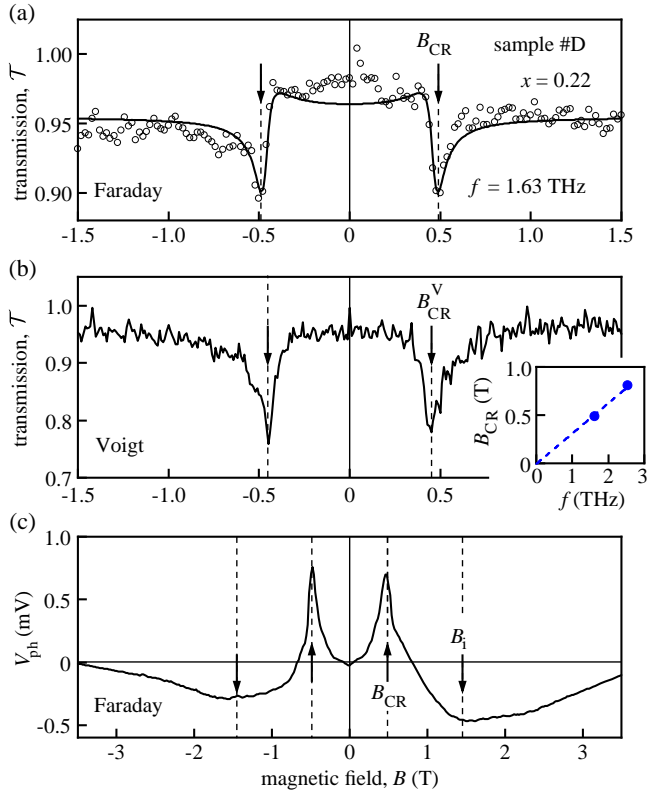
Figure 9. Normalized magnetotransmission of $f = 1.63$ THz linearly polarized radiation recorded on sample #D without band inversion ($x = 0.22$) at $T = 4.2$ K in a) Faraday and b) Voigt configurations. Solid lines in part (a) are fits using Equation (2). c) Photovoltage measured under the same conditions in Faraday configuration. The inset shows the CR field extracted from data obtained in Faraday configuration for two frequencies. All resonance field values are shown in Table 2.

Figure 10. a) Magnetotransmission of circularly polarized $f = 2.54$ THz radiation measured on sample #E with $x = 0.18$ in Faraday geometry at $T = 4.2$ K. The CR fields extracted from magnetotransmission data display a linear frequency scaling shown in the inset. b) Photovoltage measured under the same conditions for σ^- polarization. The extracted resonance field values are shown in Table 2.

magnetic field $B > 0$, most probably caused by parasitic antenna effect produced by contact wires.

4.4. Impurity-Related Resonances

Apart from the sharp CRs at low $|B|$ which constitutes the main subject of this work, all samples manifested broad resonant features at higher magnetic fields which, as discussed later, can be naturally attributed to photoionization of impurities and thus are referred here as impurity resonances. The main properties of the impurity resonances, observed in magneto-transmission as well as in photovoltage and photoconductivity, can be summarized as follows. First of all, impurity resonances appear symmetrically with respect to $B = 0$ at $B = \pm B_i$ in both Faraday and Voigt geometries, and are insensitive to the radiation helicity (Figure 4). This fact alone provides a clear evidence that they may not be caused by the CR. The resonance positions $B = \pm B_i$ scale linearly with radiation frequency, as exemplified for samples #A and #B in Figure 5b. In contrast to the CR, in which case the amplitude of dips in transmission is either independent of temperature or increases with rising T, the amplitude of dips at $B = \pm B_i$ decreases quickly with growing T and vanishes at $T \approx 30$ K (**Figure 11**a). The position B_i of impurity resonances shifts to lower $|B|$ as T grows (Figure 11b), whereas the CR positions are T-independent. The photoconductivity signal, as shown in Figure 11c, significantly increases around the position of the impurity resonance. The positions of impurity resonances for a given radiation frequency are substantially

different from those obtained on the other samples with $x = 0.15$. This is consistent with our expectations: the largest cyclotron mass is obtained for sample #D with $x = 0.22$ which is supposed to have the largest band gap, whereas the lowest mass is obtained for sample #D with $x = 0.18$, closest to the critical Cd content $x_c \simeq 0.17$ corresponding to a gapless material with a linear spectrum. We also mention that a strong asymmetry of the CR feature in Figure 10a is well captured by our fitting model and manifests significant role of interference effects included into Equation (2). Indeed, according to this formula, a symmetric shape of the transmission dip is expected either in conditions of constructive interference ($\sin \phi = 0$) or destructive interference ($\cos \phi = 0$). For intermediate values of ϕ, the shape can be highly asymmetric,[49] and the observation of such strong asymmetry is a clear indication of the importance of interference effects.

The CRs were also detected in the photovoltage response. Under linearly polarized radiation as in Figure 9c, two symmetric CR peaks emerge in positive and negative B, whereas the circularly polarized radiation in Figure 10b gives rise to a single pronounced CR peak for the corresponding active magnetic field polarity only. In this particular case, an additional peak with substantially smaller magnitude was detected for the CR passive
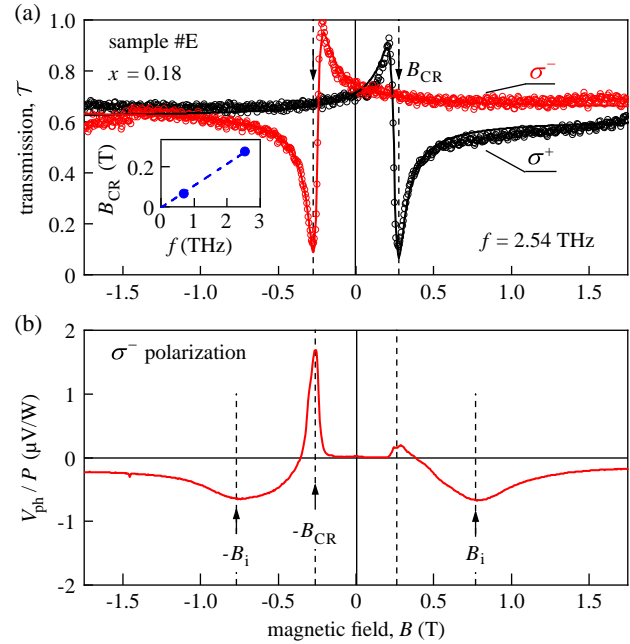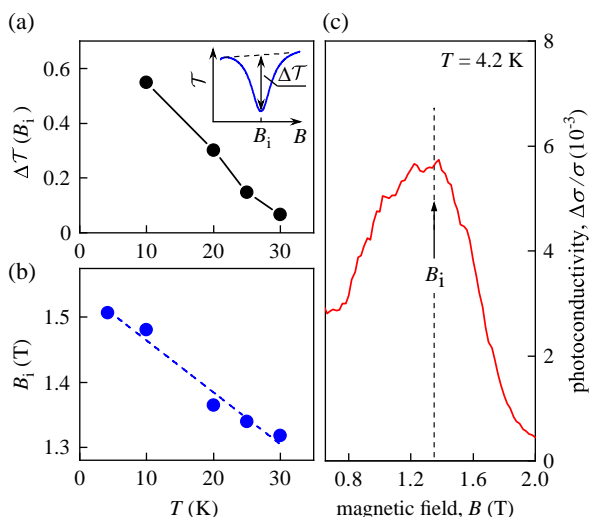
Figure 11. a) Temperature dependence of the amplitude of Lorentzian dips in magnetotransmission around the impurity resonance at $B = B_i$, extracted from data measured on sample #A at $f = 2.54$ THz as illustrated in the inset. b) Temperature dependence of the impurity resonance position B_i extracted from the same data. c) Photoconductivity $\Delta\sigma$ normalized to the dark DC conductivity σ showing a resonant peak at position $B = B_i$ of the impurity resonance. These data were obtained at $T = 4.2$ K on sample #A under $f = 2.54$ THz radiation with an applied current of 100 μA.

different for samples with different cadmium content x (Table 2). In samples with $x = 0.15$ in the flat region (with band inversion), the impurity resonances were detected both in transmission and photovoltage, whereas in samples with $x > x_c$ (without band inversion) they were present in photovoltage but not visible in magnetotransmission.

On a qualitative level, the aforementioned features are consistent with the photoionization mechanism if one considers that the activation energy of shallow impurities can significantly increase in magnetic field, an effect well-known as magnetic freeze-out of impurities.[52] In this scenario, in the limit of low B, the activation energy is so small that all impurities are thermally ionized making the photoionization processes impossible.[53] In stronger $|B|$, the activation energy of impurities increases such that at sufficiently low T the majority of impurities are in the neutral state and, at the same time, the photon energy is high enough to promote electrons into the unbound states in the conduction band. Under the same conditions, the total occupation of the conduction states is lowered making the relative contribution of the photoexcited carriers more pronounced. This is the parametric region of the impurity resonance where one expects most remarkable influence of the photoionization processes on magnetotransmission and photovoltage signals. In still stronger $|B|$ and low T, the photoionization is blocked as soon as the energy distance between the ground level of impurity and available unbound states exceeds the photon energy. Photoionization is thus possible in an intermediate range of $|B|$ centered at a certain B_i, and should be effective at sufficiently low temperatures only. Furthermore, the position of B_i should increase with the radiation frequency, and should

also be highly sensitive to temperature and to the Cd content x, as both of them modify the spectrum and, therefore, the position of impurity levels. On top of that, the temperature dependence can be affected by the processes of photoexcitation between the hydrogen-like impurity levels with subsequent thermal excitation into the continuum of unbound conduction states.[54,55]

Assuming that the resonance at B_i is related to the ionization of impurity states, it is also natural to expect different kinetics of the photoresponse with respect to that at CR. These expectations were confirmed by time-resolved photoconductivity measurements performed using a pulsed THz laser. **Figure 12** shows that indeed the decay of the photoresponse at the position $B = B_i$ of the impurity resonance is several times longer than that measured at the position $B = B_{CR}$ of CR. In the latter case (black trace in Figure 12), the photosignal essentially reproduces the form of the THz laser pulse (data not shown), meaning that kinetics of free carriers responsible for the CR is fast on the time scale of pulse duration, given by the full width at half maximum $\tau_{pulse} \simeq 100$ ns. In contrast, the photosignal measured at $B = B_i$ (red trace in Figure 12) features a significant long-time tail, which can be well fitted by an exponential function $\exp(-t/\tau)$ (blue line in Figure 12) with a decay time $\tau = 350$ ns.
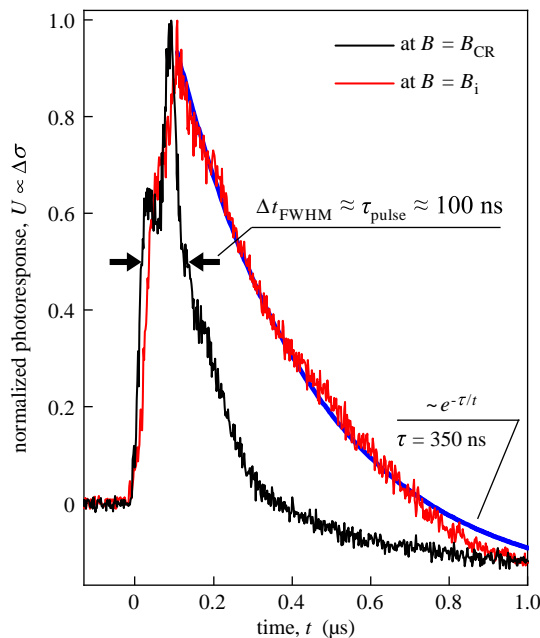

Figure 12. Time-resolved photoconductivity response $U \propto \Delta\sigma$ (normalized to its maximum value) obtained on sample #A at liquid helium temperature using a pulsed THz laser operating at $f = 2.03$ THz. The black curve demonstrates a fast photoresponse at magnetic field $B_{CR} = 0.29$ T corresponding to the CR. The full width at half maximum of the CR photoresponse, $\Delta t_{FWHM} \simeq 100$ ns, coincides with the corresponding width τ_{pulse} of the laser pulse profile (data not shown). In contrast, the photoresponse recorded at magnetic field $B_i = 1$ T, corresponding to the impurity resonance (red curve), shows a much slower decay which can be well fitted by an exponential function $\exp(-t/\tau)$ (blue line) with a decay time $\tau = 350$ ns.

5. Discussion

We now return to the main observation: a qualitatively different behavior of one of the CRs in samples with sharp and smooth interfaces between materials with and without band inversion (Sections 4.1 and 4.2). The fact that one of the CRs disappears in the Voigt geometry for sample #C with a sharp interface is a clear indicator of the true 2D nature of carriers causing this resonance. The emergence of at least one surface state is indeed guaranteed by the topologically nontrivial transition from inverted to normal band order at the interface. In Faraday geometry, the same resonance exhibits a strong temperature dependence, which additionally distinguishes it from other resonances, which are present in both Voigt and Faraday geometries and presumably originate from carriers localized at smooth interfaces. These results indicate that smooth interfaces lead to the emergence of multiple surface states, known as Volkov–Pankratov states (VPS).[16,19,56,57] As the number N of these states is not fixed by topology (apart from the requirement $N \geq 1$), their number and properties should be sensitive to a particular choice of materials, growth conditions, form of interfaces, strain profile, and so on. The dynamics of carriers occupying multiple VPS can be effectively 3D, similar to conventional quasi-2D electrons occupying multiple sub-bands in a wide quantum well, which would immediately explain our observations.

Before presenting model calculations supporting this interpretation of the distinct behaviors at smooth and sharp interfaces, we first shortly comment on the observed frequency dependencies of the CRs and on the expected difference of resonance positions in Faraday and Voigt geometries. Both aspects deserve further systematic studies but do not influence our qualitative results and conclusions, and thus are of secondary importance for the purposes of the current work.

An inspection of the results presented in Figures 5, 6, 9, 10 and Table 2 shows that the magnetic field positions of CRs in all cases fairly well follow a linear frequency dependence. These observations seemingly conflict the well-known fact that in systems with linear spectrum the energies of individual transitions between Landau levels scale as $B^{1/2}$.[58] In fact, even for massless Dirac quasiparticles, the linear dependence should approximately restore in the quasiclassical limit of high chemical potential, such that many Landau levels are occupied, and the distance between them in the vicinity of the chemical potential is well described by the cyclotron mass.[59,60] Such a classical description works well for all frequencies used in our work. Unfortunately, the presence of surface states and several types of carriers makes a reliable determination of the actual position of the chemical potential in our structures problematic. We expect that a reliable experimental evidence for the quantum square root scaling would require CR measurements in a broader frequency range.

As mentioned previously in Sections 3 and 4.1, for 3D electrons, the position of CR in Voigt geometry B_{CR}^{V} is expected to be down-shifted with respect to the CR position B_{CR} in Faraday geometry. Specifically, the resonance condition is given by $\omega^2 = \omega_p^2 + \omega_c^2$ in Voigt geometry, instead of the usual $\omega^2 = \omega_c^2$ in Faraday geometry.[48] Here, $\omega_p^2 = ne^2/m\varepsilon$ is the square of the plasma frequency of a 3D electron gas. Using for a rough estimate, the values $\varepsilon_r = \varepsilon/\varepsilon_0 \simeq 10$ for the relative permittivity and $m/m_0 = 0.004$ for the effective mass (Table 2) in the expression

$B_{CR}^{V}/B_{CR} = (1 - \omega_p^2/\omega^2)^{1/2}$, for sample #A one finds that the observed relative shifts $B_{CR}^{V}/B_{CR} \simeq 0.8$ correspond to the electron volume density $n \sim 5 \times 10^{14}\,\mathrm{cm}^{-3}$, in a reasonable agreement with estimates obtained from the analysis of magnetotransport data (Table 1). At the same time, this agreement can be a coincidence because for other samples we generally do not observe any sensible difference between the CR positions in both geometries (Table 2). These surprising findings require further analysis and focused experiments. In particular, it would be interesting to understand how such plasmonic shifts are modified in the relevant case of a quasi-2D system involving several populated 2D sub-bands at the interface.

The surface states in systems with sharp interfaces are well studied for strained HgTe films.[9,25,61,62] These topologically protected states are caused by the inversion of Γ_6 and Γ_8 bands at the interface. The energy of the surface states depends on the wave vector $\boldsymbol{k}_\parallel$ in the interface plane and lies in the interval between the corresponding energy levels of the light and heavy holes.[9,63] If the crystal is strained, there is a gap between the light- and heavy-hole sub-bands; the energy of the lowest $k_\parallel = 0$ topological surface state coincides with the top of the heavy-hole sub-band, whereas in the limit $|k_\parallel| \to \infty$ the dispersion of the high-energy surface states approaches that of the light holes. As a result, ideally, the low-temperature transport properties of a strained HgTe film with the Fermi energy lying in the gap between the light- and heavy-hole sub-bands should be solely determined by the topologically protected surface states because
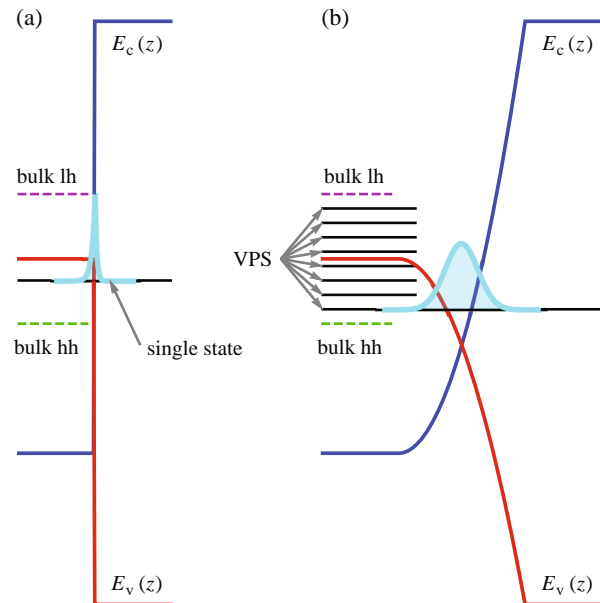

Figure 13. Illustration of the edge states forming at a) sharp and b) smooth interfaces. Light blue lines with filled area below them show the calculated probability density distributions for the edge states in both cases. The sharp interface hosts a single well-localized topologically protected state, whereas the smooth interface gives rise to multiple VPS, which are weakly localized in space. Red and blue lines show the real space profiles $E_v(z)$ and $E_c(z)$ of the corresponding band edges. The edge states emerge in the range between energies of the bulk light and heavy holes, which are shown by green and magenta dashed lines and are marked as "bulk lh" and "bulk hh," correspondingly.

all bulk states in this case are gapped. Here, it is important to mention that, despite the very existence of a topological surface state stems from the inversion of light-hole band and conduction band at the interface, the dispersion of the surface states is strongly affected by hybridization with the heavy holes. CdHgTe films with band inversion share the aforementioned qualitative properties of strained HgTe films, but usually feature much smaller band gaps which are controlled by the Cd content of the alloy.

For a smooth interface between materials with and without band inversion, the situation is different. The calculations below show that instead of a single topologically protected state, the interface now can host multiple VPS.[16,19,56,57] Similar to the case of the sharp interface, the energies of VPS lie in between the energies of the strain-split light and heavy holes. **Figure 13** schematically shows a sharp interface (as in sample #C, Figure 13a) and a smooth interface (as in sample #A or #B, Figure 13b). The left parts in Figure 13a,b present the flat $Cd_{0.15}Hg_{0.85}Te$ regions, whereas the middle parts show the transition to the top cap layer without band inversion and with a larger band gap sketched in the right parts. For the sharp interface, the spatial extension of the topologically protected surface state is determined by an exponential decay of the wave function inside both the film and the barrier. In contrast, the extension of VPS localized at a smooth interface is governed by the spatial gradient of the band gap near the band inversion point. The spatial distribution of the probability densities for the corresponding wave functions is illustrated in Figure 13. If one increases the width of the transition region between the topological insulator and normal insulator, both the total number of the VPS and their widths increase. This explains why two samples #A and #C with an almost identical design, but different interface structures, show different behavior in the Voigt configuration. Sample #C hosts 2D topologically protected states which do not experience CR in an in-plane of the interface magnetic field, whereas sample #A exhibits behavior typical for a quasi-2D system with many occupied sub-bands.

For numerical calculations, we implemented the six-band Kane model taking into account a static strain of the crystal which causes a splitting of the heavy- and light-hole sub-bands. In the basis of the Γ_6 and Γ_8 states, the Kane Hamiltonian has the form[64]

$$H = \begin{pmatrix} E_c I_2 & H_{cv} \\ H_{cv}^\dagger & E_v I_4 + H_{BP} \end{pmatrix} \tag{3}$$

where I_n is the $n \times n$ identity matrix and

$$H_{cv}^\dagger = P_{cv} \begin{pmatrix} -\frac{k_x - ik_y}{\sqrt{2}} & 0 \\ \sqrt{\frac{2}{3}}k_z & -\frac{k_x - ik_y}{\sqrt{6}} \\ \frac{k_x + ik_y}{\sqrt{6}} & \sqrt{\frac{2}{3}}k_z \\ 0 & \frac{k_x + ik_y}{\sqrt{2}} \end{pmatrix} \tag{4}$$

Here P_{cv} is the Kane parameter and H_{BP} is the Bir–Pikus Hamiltonian. To phenomenologically model the gap between light and heavy holes, we introduce a nonzero u_{zz} component of the strain tensor, in which case the Bir–Pikus Hamiltonian has the form $H_{BP} = bu_{zz} \, \text{diag}(-1, 1, 1, -1)$, where b is the valence band deformation potential and diag stands for a diagonal matrix. In the following, we set u_{zz} such that the heavy-hole sub-band is below the light-hole sub-band. This Hamiltonian for the bulk CdHgTe has three double-degenerate eigenstates: the light-hole sub-band states with dispersion $\varepsilon_l(k)$ on top, the dispersionless states in the heavy-hole sub-band $\varepsilon_h(k)$ below them, and the low-lying conduction band states $\varepsilon_c(k)$, explicitly given by

$$\varepsilon_{l,c}(k) = E_0 \pm \sqrt{\delta^2 + 2P_{cv}^2 k^2/3}$$

and

$$\varepsilon_h(k) = E_v - bu_{zz}$$

with $2E_0 = E_v + bu_{zz} + E_c$ and $2\delta = E_v + bu_{zz} - E_c$.

To calculate the VPS spectrum and wave functions for a smooth interface, we take into account the dependence of E_c and E_v on the coordinate. Using the parameters $2m_0(P_{cv}/\hbar)^2 = 18.8\,\text{eV}$,[65] the band gap $E_c - E_v = -32\,\text{meV}$ for $Cd_{0.15}Hg_{0.85}Te$,[66] and the dependencies of $E_c(z)$ and $E_v(z)$ found from the profile of compound distribution x shown in Figure 1a, we calculated the VPS for sample #A. In this calculation, we set $bu_{zz} = 2\,\text{meV}$ and add a static electric field $E = 2\,\text{kV cm}^{-1}$ at the band closing. At $k_\parallel = 0.02\,\text{nm}^{-1}$, such calculation yields three VPS with energies 3, 5, and 8 meV with respect to the heavy-hole energy at the Γ point in the $Cd_{0.15}Hg_{0.85}Te$ film. The probability density of the VPS is distributed over hundreds of nanometers, which is greater or of the order of the cyclotron radius r_c of charge carriers in the bulk CdHgTe film. The latter can be found as $r_c = v/\omega$ using $\omega = 2\pi f$ and an estimate $v = \sqrt{2/3}P_{cv}/\hbar \simeq 10^8\,\text{cm s}^{-1}$ for the carrier velocity. This yields the values of $r_c = 65$, 100, and 240 nm for $f = 2.54$, 1.63, and 0.69 THz, respectively. We also find that the number of VPS emerging at such a smooth interface is highly sensitive to variation of the band gap, as well as to the energy splitting between light- and heavy-holes caused by deformation and the static electric field. The latter parameters are not known precisely and are introduced here as phenomenological parameters. Taken together, the presented calculations confirm that smooth interfaces in our samples can indeed host many VPS leading to a quasi-2D behavior of the CRs, which are thus present for both in-plane and out-of-plane orientations of the magnetic field.

6. Conclusion

To summarize, the presented low-temperature THz spectroscopy studies of CRs in thick films of $Cd_xHg_{1-x}Te$ unambiguously show that 2D surface states are present only in structures with a sharp interface separating the internal layer with band inversion ($x < 0.17$) and a cap layer without band inversion. In contrast, conventional smooth interfaces between materials with and without band inversion, involving regions of $Cd_xHg_{1-x}Te$ with gradually changing Cd content x, make the surface states effectively 3D such that the corresponding CRs are clearly visible even for an in-plane orientation of the applied magnetic field. Our observations, supported by the calculations describing the formation of the surface states in films with sharp

and smooth interfaces, clearly demonstrate that future studies of topologically protected surface states in $Cd_xHg_{1-x}Te$ films require the structures with sharp interfaces. Apart from the CRs, all samples manifest broad helicity-independent resonances which emerge at higher magnetic fields and show slower kinetics and higher temperature sensitivity. These broad resonances are attributed to photoionization and magnetic freeze-out of impurity states.

Acknowledgements

Conflict of Interest

The authors declare no conflict of interest.

Keywords

[1] B. A. Bernevig, T. L. Hughes, S. C. Zhang, *Science* **2006**, *314*, 1757.
[2] M. König, H. Buhmann, L.W. Molenkamp, T. Hughes, C. X. Liu, X. L. Qi, S. C. Zhang, *J. Phys. Soc. Jpn.* **2008**, *77*, 031007.
[3] M. Z. Hasan, C. L. Kane, *Rev. Mod. Phys.* **2010**, *82*, 3045.
[4] J. E. Moore, *Nature* **2010**, *464*, 194.
[5] X. L. Qi, S. C. Zhang, *Rev. Mod. Phys. 83*, **2011**, 1057.
[6] *Topological Insulators: Fundamentals and Perspectives* (Eds: F. Ortmann, S. Roche, S. O. Valenzuela), Wiley-VCH, Weinheim, Germany **2015**.
[7] L. Maier, J. B. Oostinga, D. Knott, C. Brüne, P. Virtanen, G. Tkachov, E. M. Hankiewicz, C. Gould, H. Buhmann, L. W. Molenkamp, *Phys. Rev. Lett.* **2012**, *109*, 186806.
[8] H. Ren, F. Pientka, S. Hart, A. T. Pierce, M. Kosowsky, L. Lunczer, R. Schlereth, B. Scharf, E. M. Hankiewicz, L.W. Molenkamp, B. I. Halperin, A. Yacoby, *Nature* **2019**, *569*, 93.
[9] C. Brüne, C. X. Liu, E. G. Novik, E. M. Hankiewicz, H. Buhmann, Y. L. Chen, X. L. Qi, Z. X. Shen, S. C. Zhang, L.W. Molenkamp, *Phys. Rev. Lett.* **2011**, *106*, 126803.
[10] K. C. Nowack, E. M. Spanton, M. Baenninger, M. König, J. R. Kirtley, B. Kalisky, C. Ames, P. Leubner, C. Brüne, H. Buhmann, L.W. Molenkamp, D. Goldhaber-Gordon, K. A. Moler, *Nat. Mater.* **2013**, *12*, 787.
[11] D. A. Kozlov, Z. D. Kvon, E. B. Olshanetsky, N. N. Mikhailov, S. A. Dvoretsky, D. Weiss, *Phys. Rev. Lett.* **2014**, *112*, 196801.
[12] C. Brüne, C. Thienel, M. Stuiber, J. Böttcher, H. Buhmann, E. G. Novik, C. X. Liu, E. M. Hankiewicz, L.W. Molenkamp, *Phys. Rev. X* **2014**, *4*, 041045.
[13] E. Olshanetsky, Z. Kvon, G. Gusev, A. Levin, O. Raichev, N. Mikhailov, S. Dvoretsky, *Phys. Rev. Lett.* **2015**, *114*, 126802.
[14] E.Y. Ma, M. R. Calvo, J. Wang, B. Lian, M. Mühlbauer, C. Brüne, Y. T. Cui, K. Lai, W. Kundhikanjana, Y. Yang, M. Baenninger, M. König, C. Ames, H. Buhmann, P. Leubner, L.W. Molenkamp, S. C. Zhang, D. Goldhaber-Gordon, M. A. Kelly, Z. X. Shen, *Nat. Commun.* **2015**, *6*, 7252.
[15] D. Kozlov, D. Bauer, J. Ziegler, R. Fischer, M. Savchenko, Z. Kvon, N. Mikhailov, S. Dvoretsky, D. Weiss, *Phys. Rev. Lett.* **2016**, *116*, 166802.
[16] A. Inhofer, S. Tchoumakov, B. A. Assaf, G. Fève, J. M. Berroir, V. Jouffrey, D. Carpentier, M. O. Goerbig, B. Plaçais, K. Bendias, D. M. Mahler, E. Bocquillon, R. Schlereth, C. Brüne, H. Buhmann, L. W. Molenkamp, *Phys. Rev. B* **2017**, *96*, 195104.
[17] H. Maier, J. Ziegler, R. Fischer, D. Kozlov, Z. D. Kvon, N. Mikhailov, S. A. Dvoretsky, D. Weiss, *Nat. Commun.* **2017**, *8*, 2023.
[18] S. Imhof, C. Berger, F. Bayer, J. Brehm, L.W. Molenkamp, T. Kiessling, F. Schindler, C. H. Lee, M. Greiter, T. Neupert, R. Thomale, *Nat. Phys.* **2018**, *14*, 925.
[19] D. M. Mahler, J. B. Mayer, P. Leubner, L. Lunczer, D. D. Sante, G. Sangiovanni, R. Thomale, E. M. Hankiewicz, H. Buhmann, C. Gould, L.W. Molenkamp, *Phys. Rev. X* **2019**, *9*, 031034.
[20] Z. D. Kvon, S. N. Danilov, D. A. Kozlov, C. Zoth, N. N. Mikhailov, S. A. Dvoretskii, S. D. Ganichev, *JETP Lett.* **2012**, *94*, 816.
[21] M. Zholudev, F. Teppe, M. Orlita, C. Consejo, J. Torres, N. Dyakonova, M. Czapkiewicz, J. Wróbel, G. Grabecki, N. Mikhailov, S. Dvoretskii, A. Ikonnikov, K. Spirin, V. Aleshkin, V. Gavrilenko, W. Knap, *Phys. Rev. B* **2012**, *86*, 205420.
[22] P. Olbrich, C. Zoth, P. Vierling, K. M. Dantscher, G.V. Budkin, S. A. Tarasenko, V.V. Bel'kov, D. A. Kozlov, Z. D. Kvon, N. N. Mikhailov, S. A. Dvoretsky, S. D. Ganichev, *Phys. Rev. B* **2013**, *87*, 235439.
[23] A. Shuvaev, A. Pimenov, G.V. Astakhov, M. Mühlbauer, C. Brüne, H. Buhmann, and L.W. Molenkamp, *Appl. Phys. Lett.* **2013**, *102*, 241902.
[24] M. Pakmehr, C. Bruene, H. Buhmann, L.W. Molenkamp, A.V. Stier, B. D. McCombe, *Phys. Rev. B* **2014**, *90*, 235414.
[25] K. M. Dantscher, D. A. Kozlov, P. Olbrich, C. Zoth, P. Faltermeier, M. Lindner, G.V. Budkin, S. A. Tarasenko, V.V. Bel'kov, Z. D. Kvon, N. N. Mikhailov, S. A. Dvoretsky, D. Weiss, B. Jenichen, S. D. Ganichev, *Phys. Rev. B* **2015**, *92*, 165314.
[26] A. Shuvaev, V. Dziom, Z. Kvon, N. Mikhailov, A. Pimenov, *Phys. Rev. Lett.* **2016**, *117*, 1174011.
[27] K. M. Dantscher, D. A. Kozlov, M. T. Scherr, S. Gebert, J. Bärenfänger, M.V. Durnev, S. A. Tarasenko, V.V. Bel'kov, N. N. Mikhailov, S. A. Dvoretsky, Z. D. Kvon, J. Ziegler, D. Weiss, S. D. Ganichev, *Phys. Rev. B* **2017**, *95*, 201103(R).
[28] V. Dziom, A. Shuvaev, A. Pimenov, G.V. Astakhov, C. Ames, K. Bendias, J. Böttcher, G. Tkachov, E. M. Hankiewicz, C. Brüne, H. Buhmann, L.W. Molenkamp, *Nat. Commun.* **2017**, *8*, 15197.
[29] A. Kadykov, S. Krishtopenko, B. Jouault, W. Desrat, W. Knap, S. Ruffenach, C. Consejo, J. Torres, S. Morozov, N. Mikhailov, S. Dvoretskii, F. Teppe, *Phys. Rev. Lett.* **2018**, *120*, 086401.
[30] J. Gospodarič, V. Dziom, A. Shuvaev, A. A. Dobretsova, N. N. Mikhailov, Z. D. Kvon, and A. Pimenov, *Phys. Rev. B* **2019**, *99*, 115130.
[31] N. N. Berchenko, M.V. Pashkovskii, *Sov. Phys. Usp.* **1976**, *19*, 462.
[32] M. Orlita, D. M. Basko, M. S. Zholudev, F. Teppe, W. Knap, V. I. Gavrilenko, N. N. Mikhailov, S. A. Dvoretskii, P. Neugebauer,

C. Faugeras, A. L. Barra, G. Martinez, M. Potemski, *Nat. Phys.* **2014**, *10*, 233.

[33] F. Teppe, M. Marcinkiewicz, S. S. Krishtopenko, S. Ruffenach, C. Consejo, A. M. Kadykov, W. Desrat, D. But, W. Knap, J. Ludwig, S. Moon, D. Smirnov, M. Orlita, Z. Jiang, S.V. Morozov, V. Gavrilenko, N. N. Mikhailov, S. A. Dvoretskii, *Nat. Commun.* **2016**, *7*, 12576.

[34] D. Yavorskiy, K. Karpierz, M. Baj, M. Bąk, N. Mikhailov, S. Dvoretsky, V. Gavrilenko, W. Knap, F. Teppe, J. Lusakowski, *Sensors* **2018**, *18*, 4341.

[35] D. B. But, M. Mittendorff, C. Consejo, F. Teppe, N. N. Mikhailov, S. A. Dvoretskii, C. Faugeras, S. Winnerl, M. Helm, W. Knap, M. Potemski, M. Orlita, *Nat. Photonics* **2019**, *13*, 783.

[36] G. Tomaka, J. Grendysa, M. Marchewka, P. Sliz, C. Becker, A. Stadler, E. Sheregii, *Opto-Electron. Rev.* **2017**, *25*, 188.

[37] A. V. Galeeva, A. I. Artamkin, A. S. Kazakov, S. N. Danilov, S. A. Dvoretskiy, N. N. Mikhailov, L. I. Ryabova, D. R. Khokhlov, *Beilstein J. Nanotechnol.* **2018**, *9*, 1035.

[38] S. Candussio, G. V. Budkin, M. Otteneder, D. A. Kozlov, I. A. Dmitriev, V. V. Bel'kov, Z. D. Kvon, N. N. Mikhailov, S. A. Dvoretsky, S. D. Ganichev, *Phys. Rev. Mater.* **2019**, *3*, 054205.

[39] M. Otteneder, I. A. Dmitriev, S. Candussio, M. L. Savchenko, D. A. Kozlov, V.V. Bel'kov, Z. D. Kvon, N. N. Mikhailov, S. A. Dvoretsky, S. D. Ganichev, *Phys. Rev. B* **2018**, *98*, 245304.

[40] Z. D. Kvon, E. B. Olshanetsky, D. A. Kozlov, N. N. Mikhailov, S. A. Dvoretskii, *JETP Lett.* **2008**, *87*, 502.

[41] M. L. Savchenko, D. A. Kozlov, N. N. Vasilev, Z. D. Kvon, N. N. Mikhailov, S. A. Dvoretsky, A. V. Kolesnikov, *Phys. Rev. B* **2019**, *99*, 195423.

[42] P. Olbrich, J. Karch, E. L. Ivchenko, J. Kamann, B. März, M. Fehrenbacher, D. Weiss, S. D. Ganichev, *Phys. Rev. B* **2011**, *83*, 165320.

[43] S. D. Ganichev, U. Rössler, W. Prettl, E. L. Ivchenko, V.V. Bel'kov, R. Neumann, K. Brunner, G. Abstreiter, *Phys. Rev. B* **2002**, *66*, 075328.

[44] S. D. Ganichev, S. N. Danilov, V.V. Bel'kov, E. L. Ivchenko, M. Bichler, W. Wegscheider, D. Weiss, W. Prettl, *Phys. Rev. Lett.* **2002**, *88*, 057401.

[45] W. Weber, L. E. Golub, S. N. Danilov, J. Karch, C. Reitmaier, B. Wittmann, V.V. Bel'kov, E. L. Ivchenko, Z. D. Kvon, N. Q. Vinh, A. F. G. van der Meer, B. Murdin, S. D. Ganichev, *Phys. Rev. B* **2008**, *77*, 245304.

[46] C. Drexler, N. Dyakonova, P. Olbrich, J. Karch, M. Schafberger, K. Karpierz, Y. Mityagin, M. B. Lifshits, F. Teppe, O. Klimenko, Y. M. Meziani,W. Knap, S. D. Ganichev, *J. Appl. Phys.* **2012**, *111*, 124504.

[47] D. A. Kozlov, Z. D. Kvon, N. N. Mikhailov, S. A. Dvoretskii, J. C. Portal, *JETP Lett.* **2011**, *93*, 170.

[48] D. Tanner, *Optical Effects in Solids*, Cambridge University Press, Cambridge, UK **2019**.

[49] G. Abstreiter, J. P. Kotthaus, J. F. Koch, G. Dorda, *Phys. Rev. B* **1976**, *14*, 2480.

[50] T. Herrmann, I. A. Dmitriev, D. A. Kozlov, M. Schneider, B. Jentzsch, Z. D. Kvon, P. Olbrich, V.V. Bel'kov, A. Bayer, D. Schuh, D. Bougeard, T. Kuczmik, M. Oltscher, D. Weiss, and S. D. Ganichev, *Phys. Rev. B* **2016**, *94*, 081301.

[51] C. Rigaux, in *Narrow Gap Semiconductors Physics and Applications*, Springer, Berlin, Heidelberg **1980**, pp. 110–124.

[52] M. I. Dyakonov, A. L. Efros, D. L. Mitchell, *Phys. Rev.* **1969**, *180*, 813.

[53] V. J. Goldman, H. D. Drew, M. Shayegan, D. A. Nelson, *Phys. Rev. Lett.* **1986**, *56*, 968.

[54] T. M. Lifshitz, Y. F. Nad, *Dokl. Akad. Nauk SSSR* **1965**, *162*, 801 [*Sov. Phys.-Doklady* **1965**, *10*, 532].

[55] E. M. Gershenzon, G. N. Gol'tsman, N. G. Ptitsina, *Zh. Eksp. Teor. Fiz.* **1973**, *64*, 587 [*Sov. Phys. JETP* **1973**, *37*, 299].

[56] B. Volkov, O. Pankratov, *Pis'ma Zh. Eksp. Teor. Fiz.* **1985**, *42*, 145 [JETP Lett. 42, 178 (1985)].

[57] S. Tchoumakov, V. Jouffrey, A. Inhofer, E. Bocquillon, B. Plaçais, D. Carpentier, M. O. Goerbig, *Phys. Rev. B* **2017**, *96*, 201302.

[58] M. L. Sadowski, G. Martinez, M. Potemski, C. Berger, W. A. de Heer, *Phys. Rev. Lett.* **2006**, *97*, 266405.

[59] A. M. Witowski, M. Orlita, R. Stepniewski, A. Wysmołek, J. M. Baranowski,W. Strupinski, C. Faugeras, G. Martinez, M. Potemski, *Phys. Rev. B* **2010**, *82*, 165305.

[60] U. Briskot, I. A. Dmitriev, A. D. Mirlin, *Phys. Rev. B* **2013**, *87*, 195432.

[61] J. N. Hancock, J. L. M. van Mechelen, A. B. Kuzmenko, D. van der Marel, C. Brüne, E. G. Novik, G.V. Astakhov, H. Buhmann, L.W. Molenkamp, *Phys. Rev. Lett.* **2011**, *107*, 136803.

[62] O. V. Kibis, O. Kyriienko, I. A. Shelykh, *New J. Phys.* **2019**, *21*, 043016.

[63] O. A. Pankratov, S.V. Pakhomov, B. A. Volkov, *Solid State Commun.* **1987**, *61*, 93.

[64] G. Bir, G. Pikus, *Symmetry and Strain-Induced Effects in Semiconductors*, Wiley, New York, NY **1974**.

[65] E. G. Novik, A. Pfeuffer-Jeschke, T. Jungwirth, V. Latussek, C. R. Becker, G. Landwehr, H. Buhmann, L.W. Molenkamp, *Phys. Rev. B* **2005**, *72*, 035321.

[66] J. P. Laurenti, J. Camassel, A. Bouhemadou, B. Toulouse, R. Legros, A. Lusson, *J. Appl. Phys.* **1990**, *67*, 6454.